

University of Nebraska - Lincoln

From the Selected Works of Serge Youri Kalmykov

Spring April 2, 2010

Formation of Optical Bullets in Laser-Driven Plasma Bubble Accelerators

Peng Dong
Steven A. Reed
Sunghwan A. Yi
Serguei Y. Kalmykov
Gennady Shvets, et al.



Available at: https://works.bepress.com/serguei_kalmykov/12/

Formation of Optical Bullets in Laser-Driven Plasma Bubble Accelerators

Peng Dong, S. A. Reed, S. A. Yi, S. Kalmykov, G. Shvets, and M. C. Downer*

Department of Physics, University of Texas at Austin, Austin, Texas 78712-1081, USA

N. H. Matlis and W. P. Leemans

Lawrence Berkeley National Laboratory, 1 Cyclotron Road, Berkeley, California 94720, USA

C. McGuffey, S. S. Bulanov, V. Chvykov, G. Kalintchenko, K. Krushelnick, A. Maksimchuk, T. Matsuoka,

A. G. R. Thomas, and V. Yanovsky

Center for Ultrafast Optical Science, University of Michigan, 2200 Bonisteel Blvd, Ann Arbor, Michigan 48109-2099, USA

(Received 3 September 2009; published 29 March 2010)

Electron density bubbles—wake structures generated in plasma of density $\bar{n}_e \sim 10^{19} \text{ cm}^{-3}$ by the light pressure of intense ultrashort laser pulses—are shown to reshape weak copropagating probe pulses into optical “bullets.” The bullets are reconstructed using frequency-domain interferometric techniques in order to visualize bubble formation. Bullets are confined in three dimensions to plasma-wavelength size, and exhibit higher intensity, broader spectrum and flatter temporal phase than surrounding probe light, evidence of their compression by the bubble. Bullets observed at $0.8 \lesssim \bar{n}_e \lesssim 1.2 \times 10^{19} \text{ cm}^{-3}$ provide the first observation of bubble formation below the electron capture threshold. At higher \bar{n}_e , bullets appear with high shot-to-shot stability together with relativistic electrons that vary widely in spectrum, and help relate bubble formation to fast electron generation.

DOI: [10.1103/PhysRevLett.104.134801](https://doi.org/10.1103/PhysRevLett.104.134801)

PACS numbers: 41.75.Jv, 42.40.-i, 52.38.Kd

The idea of accelerating charged particles to relativistic energy by surfing them on charge density waves propagating at light speed through centimeter-length underdense plasma in the wake of an intense ultrashort laser pulse was proposed 30 years ago [1]. Now such laser-plasma accelerators (LPAs) produce low-emittance [2] electron bunches with low energy spread and central energy up to 1 GeV [3]. One important approach to producing such high-quality bunches and scaling them to multi-GeV energy in the future [4] while using laser power efficiently is to enable the drive pulse to self-focus and self-compress during its initial nonlinear interaction with the plasma [5], thereby increasing its peak intensity. The ponderomotive force of the pulse can then blow out electrons completely from its immediate wake, creating a bubble [6] that guides the drive pulse stably over multiple Rayleigh lengths [7]. If the bubble expands and contracts rapidly enough in diameter, it can trap, accelerate and collimate electrons with exceptional uniformity [8].

Early LPA experiments [9–11] in the bubble regime focused on characterizing the quasimonoenergetic electrons that the accelerator produced, leaving analysis of the complex nonlinear physics of drive pulse focusing and compression, bubble formation and evolution, electron injection and acceleration, and drive pulse guiding and depletion to intensive computer simulations [12] based on estimated initial conditions. Full understanding, optimization, and scaling of bubble-regime LPAs, however, requires direct *in situ* characterization of the accelerator structure itself, independently of generated electrons. Accordingly, recent experiments began to characterize the

bubble directly through its backreaction (focusing, scattering, frequency broadening) on the drive pulse [5,7]. In these experiments the drive pulse overlaps only a small portion of the accelerator structure and, because of its relativistic intensity, is phase modulated by processes (e.g., relativistic electron mass increase) unrelated to the accelerator structure itself. Here, to overcome these limitations, we characterize plasma bubbles through their guiding, compression, and phase modulation of a copropagating weak probe pulse that overlaps the entire accelerating structure. By imaging the bubble-modulated probe from the plasma exit and spectrally interfering it with a copropagating reference pulse, we reconstruct its spatiotemporal profile, enabling snapshotlike visualization of the guiding and compression action of the plasma bubble. We previously employed similar methods to visualize weakly nonlinear sinusoidal wakes in plasmas of average density $\bar{n}_e < 0.6 \times 10^{19} \text{ cm}^{-3}$ that produced few or no relativistic electrons [13]. Here we address the more important, albeit more challenging, task of visualizing highly nonlinear wakes in plasmas of density $10^{19} \lesssim \bar{n}_e \lesssim 3 \times 10^{19} \text{ cm}^{-3}$ that can produce high-quality relativistic electron beams.

Nonlinear wakes were created by focusing ~ 30 TW, 800 nm wavelength, 30 fs FWHM linearly polarized pulses from the University of Michigan’s HERCULES laser to spot radius $w_0 \approx 10 \mu\text{m}$ (Rayleigh length $Z_R \approx 0.4$ mm) and normalized laser vector potential $a_0 = eA/m_e c^2 \approx 2$ at the entrance ($z = 0$) of a 2-mm supersonic He gas jet. A transverse interferometer measured electron density $\bar{n}_e(z)$ averaged over plasma oscillations vs distance z along the laser propagation axis. A magnetic spectrometer measured

energy distribution of accelerated electrons above ~ 30 MeV. To characterize pump-generated structures $n_e(r, \zeta, z)$, two additional pulses were split from the pump, frequency doubled to $\lambda_{\text{pr}} = 400$ nm, stretched to duration 1 ps, focused to spot size $w_{\text{pr}} \approx 50 \mu\text{m}$, and copropagated through the jet, polarized orthogonally to the pump. Here r denotes perpendicular distance from the propagation axis and $c\zeta$ distance behind the pump. The leading 400 nm pulse (reference) arrived before the pump; the trailing pulse (probe) extended from $-100 \text{ fs} \leq \zeta \leq 900 \text{ fs}$, overlapping the pump and its wake. Reference and probe pulses were imaged from the gas jet exit ($z_{\text{exit}} \approx 2 \text{ mm}$) to a spectrometer slit, which selected a 1D line-out and projected a frequency-domain (FD) hologram [Fig. 1(a), left] onto a CCD camera. Polarization, spatial, and frequency filtering blocked frequency-broadened pump light [7] from the spectrometer.

From the FD holograms and separate characterization of incident probe and reference pulses we recovered the FD probe electric field $E_{\text{pr}}(r, \omega, z_{\text{exit}})$. Fourier transformation (FT) of $E_{\text{pr}}(r, \omega, z_{\text{exit}})$ reconstructed its time-domain amplitude $|E_{\text{pr}}(r, \zeta, z_{\text{exit}})|$ and phase change $\Delta\phi_{\text{pr}}(r, \zeta, z_{\text{exit}})$ profiles, as in previous work [13]. When both reference and

probe arrived at the jet before the pump, FD interference fringes were straight [Fig. 1(a), left], and FT simply reconstructed the unaltered incident probe profile $|E_{\text{pr}}(r, \zeta, z_{\text{exit}})| = |E_{\text{pr}}(r, \zeta, 0)|$ [Fig. 1(a), middle] with $\Delta\phi_{\text{pr}}(r, \zeta, z_{\text{exit}}) = 0$. In previous studies of linear sinusoidal wakes in tenuous ($\bar{n}_e \sim 10^{18} \text{ cm}^{-3}$) plasma, changes in the spectral envelope of the FD hologram and in $|E_{\text{pr}}(r, \zeta, z_{\text{exit}})|$ were small, and pump-generated structures $n_e(r, \zeta)$ were recovered entirely from the $\Delta\phi_{\text{pr}}(r, \zeta, z_{\text{exit}})$ profile, a procedure we call FD holography (FDH) [13].

Here, by contrast, strongly nonlinear wakes in dense ($\bar{n}_e \geq 10^{19} \text{ cm}^{-3}$) plasma reshape the spectral envelope of the FD hologram significantly [see Figs. 1(b)–1(h), left column]. For $\bar{n}_e > 10^{19} \text{ cm}^{-3}$, one or more streaks appear to the red side of the incident probe spectrum [highlighted by brackets in Figs. 1(c)–1(h), left column]. A weak extension to the blue side was sometimes also observed, although a spectral filter inserted to block blue-shifted pump light partly suppressed this signal. Since FDH records the probe's spectral amplitude *and phase*, these generated frequencies can (upon FT) be identified with their creation point within the *temporal* profile $|E_{\text{pr}}(r, \zeta)|$. Indeed, $|E_{\text{pr}}(r, \zeta)|$ distorts from its incident profile [see Figs. 1(b)–1(h), middle column]. Moderate distortion is evident already at $\bar{n}_e = 0.4 \times 10^{19} \text{ cm}^{-3}$ [Fig. 1(b), middle]. For $\bar{n}_e > 0.8 \times 10^{19} \text{ cm}^{-3}$, an intense bright spot forms near the probe leading edge at the same r as one of the prominent redshifted streaks [Figs. 1(c)–1(h), middle, highlighted by vertical arrows], and appears prominently in all shots above this threshold. The *spectral* phase $\phi_{\text{pr}}(\omega)$ of light within this bright spot (recorded on the FD hologram) lacks detectable quadratic or higher-order dependence on ω , signifying a nearly flat *temporal* phase, in sharp contrast to the strong quadratic spectral phase (signifying linear chirp) of the remaining probe profile. The bright spot is thus a *fully compressed* subpulse embedded in the larger chirped probe profile. Such light packets, confined in 3D, are often called “optical bullets” [14]. For $0.8 \leq \bar{n}_e \leq 1.2 \times 10^{19} \text{ cm}^{-3}$, bullets appear without relativistic electrons [Figs. 1(c) and 1(d), labeled Regime I]. For higher \bar{n}_e (Regime II), they appear together with relativistic electrons, sometimes poly- [Figs. 1(e) and 1(f), right], sometimes quasi-mono-energetic [Figs. 1(g) and 1(h) right]. Simultaneously a fringe of probe light outlines ionization fronts [see, e.g., horizontal arrows in Fig. 1(c), middle].

To understand bullet formation qualitatively, consider the front end of the bubble (radius R_b) as a moving lens with internal transverse refractive index profile $\eta(r) = 1 - \omega_p^2(r)/2\omega_{\text{pr}}^2$, like, e.g., a parabolic channel with $\omega_p^2(r) = (\bar{n}_e e^2/\epsilon_0 m_e) r^2/R_b^2$. Since η peaks on axis, the channel focuses probe light to spot size σ_{bullet} over distance $f = \pi\sigma_{\text{bullet}}^2/\lambda_{\text{pr}}$ [15]. Approximating the bullet as a fundamental Gaussian guided mode yields $\sigma_{\text{bullet}} \approx (\Delta n_e \pi r_e)^{-1/2}$, where Δn_e is the density depression on axis and r_e the classical electron radius [16]. For $\Delta n_e \approx$

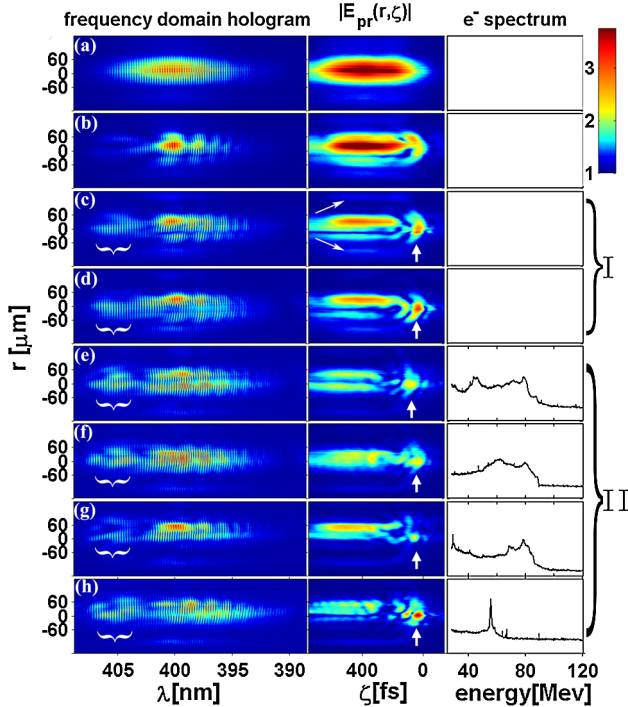


FIG. 1 (color online). Left column: Spectral interferograms at various plasma densities showing Stokes shifted streaks near $r \approx 0$ in (c)–(h) (highlighted by brackets). Middle column: reconstructed exit probe amplitude profiles: (a) undistorted profile; for (c)–(h) optical bullets (see vertical arrows) near front edge. Right column: energy spectrum of electrons produced. Regime I: bullets appear without relativistic electrons; Regime II: bullets appear with relativistic electrons. Plasma density \bar{n}_e [10^{19} cm^{-3}] in each row was (a) 0; (b) 0.4; (c) 1.0; (d) 1.2; (e) 2.6; (f) 2.6; (g) 2.6; (h) 3.2 in the doubly ionized He region.

10^{19} cm^{-3} , $\sigma_{\text{bullet}} \approx 3.4 \mu\text{m}$, and $f \approx 0.1 \text{ mm}$. Since $f \ll z_{\text{exit}}$, the bubble focuses probe light during jet transit. At the same time, reconstructed $\Delta\phi_{\text{pr}}(r, \zeta, z_{\text{exit}})$ profiles become extremely complicated, and are no longer as simply related to plasma structure as at lower \bar{n}_e [13]. This is in part because $\Delta\phi_{\text{pr}}$ often exceeds 2π , creating phase jumps that are difficult to unwrap, and in part because refraction distorts the radial distribution of $\Delta\phi_{\text{pr}}(r, \zeta, z_{\text{exit}})$. Here we focus instead on $|E_{\text{pr}}(r, \zeta, z_{\text{exit}})|$ profiles, which are reconstructed along with $\Delta\phi_{\text{pr}}(r, \zeta, z_{\text{exit}})$ as in [13], but are more simply interpreted in dense refractive plasmas. Since they resemble shadowgraphs projected on a virtual screen at z_{exit} , we call their analysis FD shadowgraphy.

To understand bullet formation quantitatively, we simulated nonlinear wake generation and copropagation of a 400 nm probe pulse in Regime I using the fully relativistic, quasistatic time-averaged particle-in-cell (PIC) code WAKE [17] in an axisymmetric geometry, taking $\bar{n}_e(z)$ from transverse interferometry. When electron injection is negligible, WAKE yields results nearly identical to the fully kinetic three-dimensional (3D) Virtual Plasma Physics Lab (VLPL) PIC code [18] (discussed below), which confirms *low charge injection* ($<40 \text{ pC}$) throughout Regime I. For these conditions, WAKE runs faster than VLPL, simulates wider transverse domain and longer propagation distances, suffers less numerical noise from particle discretization, and models field ionization of the gas accurately. Figure 2 shows density $n_e(r, \zeta, z)$ (top row) and normalized probe intensity (second row) at $z = 0.1$ (left column), 0.5 mm (center) and 1.8 mm (right column) for peak density $\bar{n}_e = 0.8 \times 10^{19} \text{ cm}^{-3}$. The bubble guides the pump (shown by red e^{-2} isointensity contours in the top row) over nonlinear pump depletion length $L_{\text{pd}} \approx (\omega_0^2/\omega_p^2)(c\tau) \approx 1.8 \text{ mm}$ limited by erosion of its leading edge [7]. At $z = 0.1 \text{ mm}$, pump and probe retain their incident Gaussian spatiotemporal profiles as a plasma wake forms. By $z = 0.5 \text{ mm}$, the pump compresses to 20 fs, ionization fronts outline the He^+ and He^{2+} regions, and electrons are blown out from the first wake bucket. Simultaneously, the first wake bucket focuses and compresses probe light initially inside it to an optical bullet. Probe radiation initially *outside* the fully formed bubble reflects from its dense walls, some of it forming a fringe outlining the ionization fronts. Near the exit ($z = 1.8 \text{ mm}$) the pump, still guided, erodes to $\sim 5 \text{ fs}$ consistent with the estimated L_{pd} , while the probe bullet remains trapped near the front of the bubble. A simulated FD hologram of the exiting probe (Fig. 2, lower left) features a frequency-broadened streak centered at $r = 0$, consistent with experimental data, that corresponds to the trapped bullet. The probe amplitude at z_{exit} reconstructed using the experimental reference bandwidth ($\Delta\lambda \approx 10 \text{ nm}$) and imaging resolution ($\sim 10 \mu\text{m}$) (Fig. 2, lower right) preserves the main features of the exiting probe with degraded resolution, in agreement with observed bullets in Figs. 1(c) and 1(d). These simulations underpin the interpretation of Regime I: a bubble forms

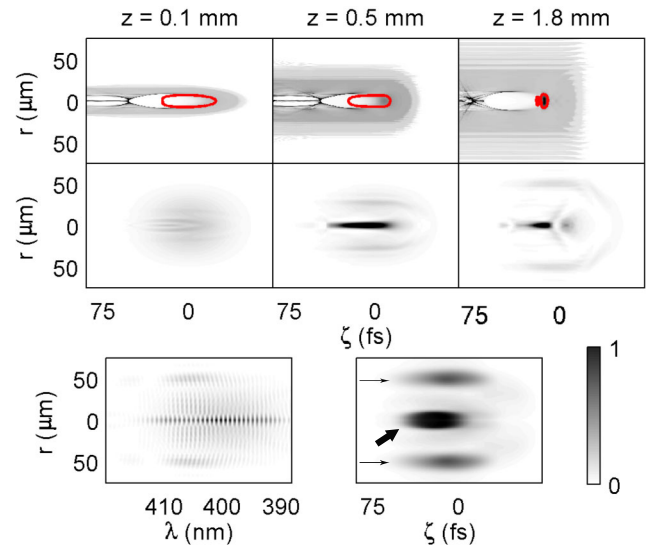


FIG. 2 (color online). WAKE simulations for $\bar{n}_e = 0.8 \times 10^{19} \text{ cm}^{-3}$ showing formation of plasma wake (top row), with pump e^{-2} isointensity contours outlined in red, and refraction of 400 nm probe (shortened to 100 fs centered on first wake bucket) to form optical bullet inside the bubble and fringe outlining ionization front (2nd row) as they propagate (left to right) from gas jet entrance (left column), to $z = 0.5 \text{ mm}$ (middle column), to near z_{exit} (right column). Bottom left: simulated FD hologram shows broadened streak at $r = 0$ corresponding to bullet inside the bubble. Bottom right: probe intensity profile reconstructed from FD hologram using experimental reference bandwidth and imaging resolution. Arrows: bullet (thick); ionization front (thin, horizontal).

below the threshold of electron capture, here observed for the first time to our knowledge.

Wake and probe pulse evolution in Regime II was simulated with VLPL [18] to account for electron injection and beam loading. Figures 3(a)–3(c) show bubble evolution in fully-ionized plasma of $\bar{n}_e = 2.3 \times 10^{19} \text{ cm}^{-3}$, while Figs. 3(e)–3(g) show the corresponding evolution of $|E_{\text{pr}}(r, \zeta, z)|$ (initial profile as for Fig. 2). By $z = 0.56 \text{ mm}$, a bubble [Fig. 3(a)] and an optical bullet spanning the bubble's length [$0 < \zeta \leq 35 \text{ fs}$, Fig. 3(e)] have formed. Trailing wake buckets ($\zeta > 35 \text{ fs}$) also trap probe light. By $z = 0.92 \text{ mm}$, massive self-injection fills the rear of the bubble with a dense electron bunch [see Fig. 3(b)]. Its space-charge force prevents the bubble from closing [19]. The trailing periodic wake then collapses, and the only *persistent* probe feature becomes an optical bullet focused in the first bucket [Fig. 3(f)]. Probe features trailing the first bucket are intermittent, and time average to negligible amplitude. By $z = 1.56 \text{ mm}$, the pump depletes and the bubble, now driven primarily by electrons, nearly triples in volume [Fig. 3(c)]. The optical bullet outruns the bubble and starts diffracting [Fig. 3(g)], which may explain formation of multiple redshifted streaks in Figs. 1(e)–1(g).

Several conclusions about bullets emerge from the combined simulations. First, the bullet forms in the first bucket

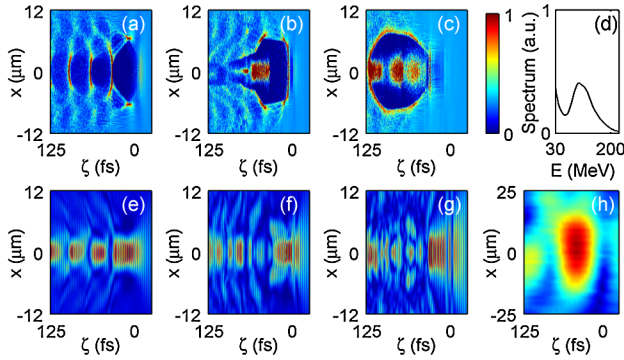


FIG. 3 (color online). VLPL simulations for $\bar{n}_e = 2.3 \times 10^{19} \text{ cm}^{-3}$. Panels (a)–(c): plots of electron density showing formation of bubble, injection of electrons [(b) and (c)] at $z = 0.56 \text{ mm}$ (left), 0.92 mm (2nd column) and 1.56 mm (3rd column); Panels (e)–(g): plots of $|E_{pr}(r, \zeta, z)|$ of the y-polarized probe at the same z values, showing optical bullet formation. Panel (d): accelerated electron spectrum at $z = 1.56 \text{ mm}$, showing quasimonoenergetic feature at 90 MeV similar to Fig. 1(g). Panel (h): Enlarged image of bullet from Fig. 1(g).

before electron self-injection starts [Fig. 3(e)], and thus outruns the electron bunch and is unaffected by bubble elongation caused by beam loading. The bullet’s length thus replicates the bubble’s length *early* in the jet (although probe bandwidth limits its measured length to $\geq 30 \text{ fs}$), and its width the blowout region width (although it appears broader because of limited imaging resolution and diffraction from the front of the bubble before $z = z_{\text{exit}}$), as seen in comparing Figs. 3(g) and 3(h). Thus the bullet “remembers” the bubble’s shape shortly after it formed. Second, the bullet interacts primarily with the bubble’s quasistatic *front* end, which both simulation codes model accurately. WAKE simulations with the same input parameters used for Fig. 3 (not shown) yield *bullet* evolution similar to 3D VLPL results over the entire interaction length, despite very different evolution of the bubble tail. Third, the simulations show the bubble’s front end is much less sensitive to changing laser-plasma conditions than its dynamic back end. This accounts for the shot-to-shot *stability* of bullet size and shape evident in the middle column of Figs. 1(c)–1(h), even while the corresponding electron spectra vary widely. Quasimonoenergetic electron spectra, as shown in Fig. 1(g) and simulated in Fig. 3(d), are common in Regime II, whereas highly monoenergetic spectra such as Fig. 1(h), never reproduced in 2 mmlong VLPL simulations, were observed occasionally. Such features with $\leq 1\%$ energy spread have been reported previously in this \bar{n}_e range [20]. In our case, they may result from occasional perturbations in the gas jet profile or prepulse excitations that cause the pump to focus near the jet exit, reducing effective interaction length below

L_{pd} . These shots also yield the most intense optical bullets [see Fig. 1(h), middle column].

In conclusion, we demonstrate that optical bullets visualize formation of laser-produced electron density bubbles robustly, and independent of wakefield-accelerated electrons. We observe for the first time the formation of stable bubbles below the threshold for production of relativistic electrons. With improvements in imaging and bandwidth, optical bullets should resolve finer details of bubble structure, and support future extensions of bubble-regime LPA to multi-GeV energies.

This work was supported by DOE grants DE-FG02-07ER54945, DE-FG02-96ER40954, DE-FG02-04ER41321, and DE-AC02-05CH11231, NSF Physics Frontier Center FOCUS (Grant PHY-011436) and NSF/DNDO Grant 0833499. The authors thank A. Pukhov for the VLPL code, and the Texas Advanced Computing Center for computing resources.

*downer@physics.utexas.edu

- [1] T. Tajima and J.M. Dawson, Phys. Rev. Lett. **43**, 267 (1979).
- [2] S. Fritzler *et al.*, Phys. Rev. Lett. **92**, 165006 (2004).
- [3] W.P. Leemans *et al.*, Nature Phys. **2**, 696 (2006); S.P.D. Mangles *et al.*, Phys. Rev. Lett. **96**, 215001 (2006); S. Karsch *et al.*, New J. Phys. **9**, 415 (2007); J. Osterhoff *et al.*, Phys. Rev. Lett. **101**, 085002 (2008); N. A. M. Hafz *et al.*, Nat. Photon. **2**, 571 (2008); S. Kneip *et al.*, Phys. Rev. Lett. **103**, 035002 (2009); D. H. Froula *et al.*, Phys. Rev. Lett. **103**, 215006 (2009).
- [4] W. Lu *et al.*, Phys. Rev. ST Accel. Beams **10**, 061301 (2007).
- [5] V. Malka *et al.*, Science **298**, 1596 (2002); A.G.R. Thomas *et al.*, Phys. Rev. Lett. **98**, 095004 (2007).
- [6] A. Pukhov and J. Meyer-ter-Vehn, Appl. Phys. B **74**, 355 (2002).
- [7] J.E. Ralph *et al.*, Phys. Rev. Lett. **102**, 175003 (2009).
- [8] S. Kalmykov *et al.*, Phys. Rev. Lett. **103**, 135004 (2009).
- [9] S.P.D. Mangles *et al.*, Nature (London) **431**, 535 (2004).
- [10] C.G.R. Geddes *et al.*, Nature (London) **431**, 538 (2004).
- [11] J. Faure *et al.*, Nature (London) **431**, 541 (2004).
- [12] F.S. Tsung *et al.*, Phys. Rev. Lett. **93**, 185002 (2004).
- [13] N.H. Matlis *et al.*, Nature Phys. **2**, 749 (2006).
- [14] Y.S. Kivshar and G.P. Agrawal, *Optical Solitons: from Fibers to Photonic Crystals* (Academic, San Diego, 2003).
- [15] A. Yariv, *Quantum Electronics* (Wiley & Sons, New York, 1975), 2nd ed.
- [16] C.G. Durfee III, J. Lynch, and H.M. Milchberg, Phys. Rev. E **51**, 2368 (1995).
- [17] P. Mora and T.M. Antonsen, Jr, Phys. Plasmas **4**, 217 (1997).
- [18] A. Pukhov, J. Plasma Phys. **61**, 425 (1999).
- [19] M. Tzoufras *et al.*, Phys. Rev. Lett. **101**, 145002 (2008).
- [20] A. Maksimchuk *et al.*, Appl. Phys. B **89**, 201 (2007); J.G. Gallacher *et al.*, Phys. Plasmas **16**, 093102 (2009).